Research Square

Preprints are preliminary reports that have not undergone peer review.
They should not be considered conclusive, used to inform clinical practice,
or referenced by the media as validated information.

Mechanism-informed prediction of complex karst water inflow: overcoming strong nonlinearity via a hybrid deep learning framework

Wenfei Chi
Hefei University of Technology
Jiazhong Qian
qianjiazhong@hfut.edu.cn
Hefei University of Technology
Yong Liu
Hefei University of Technology
Lei Ma
Hefei University of Technology
Yaping Zhang
Hefei University of Technology
Xin Zhang
Hefei University of Technology

Research Article

Keywords: Water inflow, Karst geology, Underground engineering, Self-Attention (SA), Long Short-Term Memory (LSTM)

Posted Date: March 5th, 2026

DOI: https://doi.org/10.21203/rs.3.rs-8972488/v1

License: This work is licensed under a Creative Commons Attribution 4.0 International License.
Read Full License

Additional Declarations: No competing interests reported.

Mechanism-informed prediction of complex karst water inflow: overcoming strong nonlinearity via a hybrid deep learning framework

Wenfei Chi[1], Jiazhong Qian[1*], Yong Liu[2*], Lei Ma[1], Yaping Deng[1], Xin Zhang[1]

[1]School of Resources and Environmental Engineering, Hefei University of Technology, Hefei 230009, China

[2]School of Food and Biological Engineering, Hefei University of Technology, Hefei 230601, China

***Corresponding authors:**

Jiazhong Qian

School of Resource and Environment Engineering, Hefei University of Technology, Hefei 230009, China

Tel.: +86 138 5600 7012; E-mail address: qianjiazhong@hfut.edu.cn

Yong Liu

School of Food and Biological Engineering, Hefei University of Technology, Hefei 230601, China

Tel.: +86 18919661073; E-mail address: liuyong@hfut.edu.cn

Highlights:

1. A rock mass-karst-structure identification system for water inflow mechanisms was established.
2. A CEEMDAN-based fusion model combining self-attention and LSTM was proposed.
3. The LSTM's ability to capture global dependencies was enhanced in the proposed fusion model.
4. The superior "posterior" integration strategy of self-attention was identified.

Abstract

To address the challenges of strong nonlinearity and non-stationarity in predicting water inflow in karst engineering, this study investigates an underground intake pumping station of the Shanxi Yellow River Diversion Project, systematically revealing the nonlinear causes of inflow dynamics. The research reveals that the low-permeability boundary formed by lining construction transforms karst seepage from matrix diffuse flow to conduit concentrated flow, significantly amplifying the system's pulse response to extreme meteorological forcing. Based on this mechanism, a hybrid predictive framework integrating CEEMDAN, LSTM, and a Self-Attention (SA) mechanism was developed, with a focus on comparing the predictive performance of two SA topological configurations: pre-positioned and post-positioned. Experiments confirm that the topological placement of SA significantly impacts nonlinear capture capability: when positioned subsequent to the LSTM layer as a "global feature recalibrator," it effectively compensates for the LSTM gating mechanism's "smoothing effect" on low-energy pulse signals, achieving high-fidelity capture of nonlinear abrupt change features through cross-temporal association reweighting. Results show that the post-positioned architecture achieves high accuracy with R^2 = 0.902, MAE = 0.002, and RMSE = 0.003. Compared to the pre-positioned architecture, the post-positioned configuration further reduces RMSE and MAE by approximately 50% and 67%, respectively, significantly enhancing hazard identification sensitivity in data-sparse karst regions. This provides a scientific basis for transitioning disaster prevention management from passive sealing to mechanism-driven proactive early warning.

Keywords: Water inflow; Karst geology; Underground engineering; Self-Attention (SA); Long Short-Term Memory (LSTM)

1. Introduction

Water inflow has always been a significant problem affecting the safety of underground engineering construction, characterized by its suddenness, destructiveness, and chain-reaction nature, resulting in significant casualties and property losses [1-5]. Particularly in areas with well-developed karst fissures, complex hydrogeological conditions increase the likelihood of accidents [6, 7]. In recent years, water inflow-related disasters in underground engineering have occurred in various locations worldwide [8]. Therefore, within this context, characterizing the hydromechanical drivers of water inflow and establishing an advanced predictive framework are critical to bridging the gap between theoretical geological understanding and real-time construction safety protocols.

Water inflow in underground engineering arises from complex causes closely related to the regional geological setting. It is particularly governed by key factors such as lithology, structural development, and karst development patterns [9]. It often exhibits characteristics that cause disasters, resulting from the coupling of multiple factors. Existing research indicates that the mechanisms of water inflow can be primarily categorized into two types: the first is the "geological defect type," where water inflow is directly caused by inherent geological structures such as faults and karst conduits; the second is the "intact rock mass failure type," which occurs in intact rock layers due to the combined effects of engineering excavation and groundwater pressure [10, 11]. Additionally, there exists a "hybrid type" combining both mechanisms, as well as "structurally controlled" and "non-structurally controlled" types determined by water source conditions [12]. The structural types of water inflow disasters are classified differently based on their various causes. Investigating the disaster-inducing structural types of water inflow is crucial for further summarizing the patterns and origins of water inflow.

Over the past few decades, significant research has been conducted on predicting water inflow in underground engineering using numerical and empirical methods [2]. However, these approaches are mostly suited for shallow buried projects and rely on multiple fitting parameters—such as borehole data, permeability coefficients, and groundwater levels—whose accuracy is highly data-dependent [13, 14]. Acquiring these parameters is often challenging in practice, especially in data-scarce karst mountainous regions with complex geology [15]. Currently, no well-established method exists for accurately predicting water inflow in karst underground engineering. In this context, deep learning models are considered a promising alternative [16-18].

In recent years, Artificial Neural Networks (ANNs) have significantly advanced hydrological prediction, being widely applied in rainfall-runoff modeling and flood forecasting [19-22]. A key advantage of ANNs is their ability to model non-stationary hydrological sequences without requiring detailed knowledge of the underlying physical processes, despite their "black box" nature [23].

However, traditional ANNs struggle to capture temporal dependencies in sequential data, often losing important time-related features [24, 25]. To address this, Recurrent Neural Networks (RNNs) have been developed, which transmit historical hidden states through cyclic connections. This enables RNNs to retain past information, making them particularly suitable for modeling time series data [26].

Standard RNNs are prone to vanishing or exploding gradients when processing long sequences, limiting their ability to learn long-term dependencies. To address this, Long Short-Term Memory (LSTM) networks were introduced, incorporating gating mechanisms to regulate information accumulation and forgetting, thereby improving modeling of long-range dependencies [27, 28]. As a specialized RNN designed for sequential data, LSTM has proven valuable in hydrological research [29]. For instance, Hu et al. [30] demonstrated LSTM's superior flood prediction performance compared to

an ANN, while Huang et al. [31] improved runoff prediction by incorporating physical relationships between input and output variables. Additionally, Huang et al. [32] applied LSTM to reconstruct groundwater recharge dynamics in South Australia from 1970 to 2012, thereby further confirming its effectiveness in hydrological time-series prediction.

Despite these strengths, LSTM performs inadequately with highly nonlinear sequences [33]. To improve accuracy, An et al. [17] applied Singular Spectrum Analysis and Ensemble Empirical Mode Decomposition to preprocess the original series, noting that different decomposition methods suit varying data characteristics. Similarly, Bian et al. [34] found that CEEMDAN decomposition enhanced LSTM predictions more effectively than EMD or EEMD. However, such approaches do not fully resolve LSTM's limitations in capturing long-range dependencies, resisting noise, or providing interpretability [35].

The attention mechanism enables more effective integration of key information across data segments. Combined with LSTM, it has succeeded in natural language processing and time series tasks [36]. Self-attention (SA), or internal attention, captures relevant patterns solely from the input sequence without external information [37]. Unlike traditional attention, which models dependencies between source and target sequences, SA operates within a single sequence, establishing relationships among internal elements and improving efficiency in capturing latent dependencies. Integrating self-attention with LSTM has shown promising results across industrial applications [38-40], though model performance varies significantly depending on whether SA is placed before or after the LSTM layer.

To bridge the critical gap between qualitative geological assessment and quantitative predictive intelligence in deep underground environments, this study aims to achieve two primary objectives: (1) Revealing the causative mechanisms and disaster-causing patterns of water inflow in underground engineering within the study area by analyzing characteristics including surrounding rock strength, rock permeability, geological structures, and karst development; (2) Diagnosing the optimal integration strategy for the Self-Attention (SA) mechanism within a recurrent architecture is essential for decoding the 'physical fingerprints' concealed in univariate inflow sequences.

2. Study area and data

The Xiaolangdi Yellow River Diversion Underground Pump Station is located in Yuanqu County, Yuncheng City, Shanxi Province, on the left bank of the Banjian River, a tributary of the Yellow River (Fig. 1a). The slope area of the site exhibits multiple bedrock outcrops. The Banjian River flows from east to west through the valley at the base of the ridge, with an elevation of 280-285 meters at the valley bottom. The terrain in this region consists of low, gentle hills, with a basement primarily composed of thick Ordovician (O) carbonate rock formations, overlain by Carboniferous (C) quartz sandstone layers. The bedrock strata strike NE16~39 ° and dip southeast (Fig. 1b).

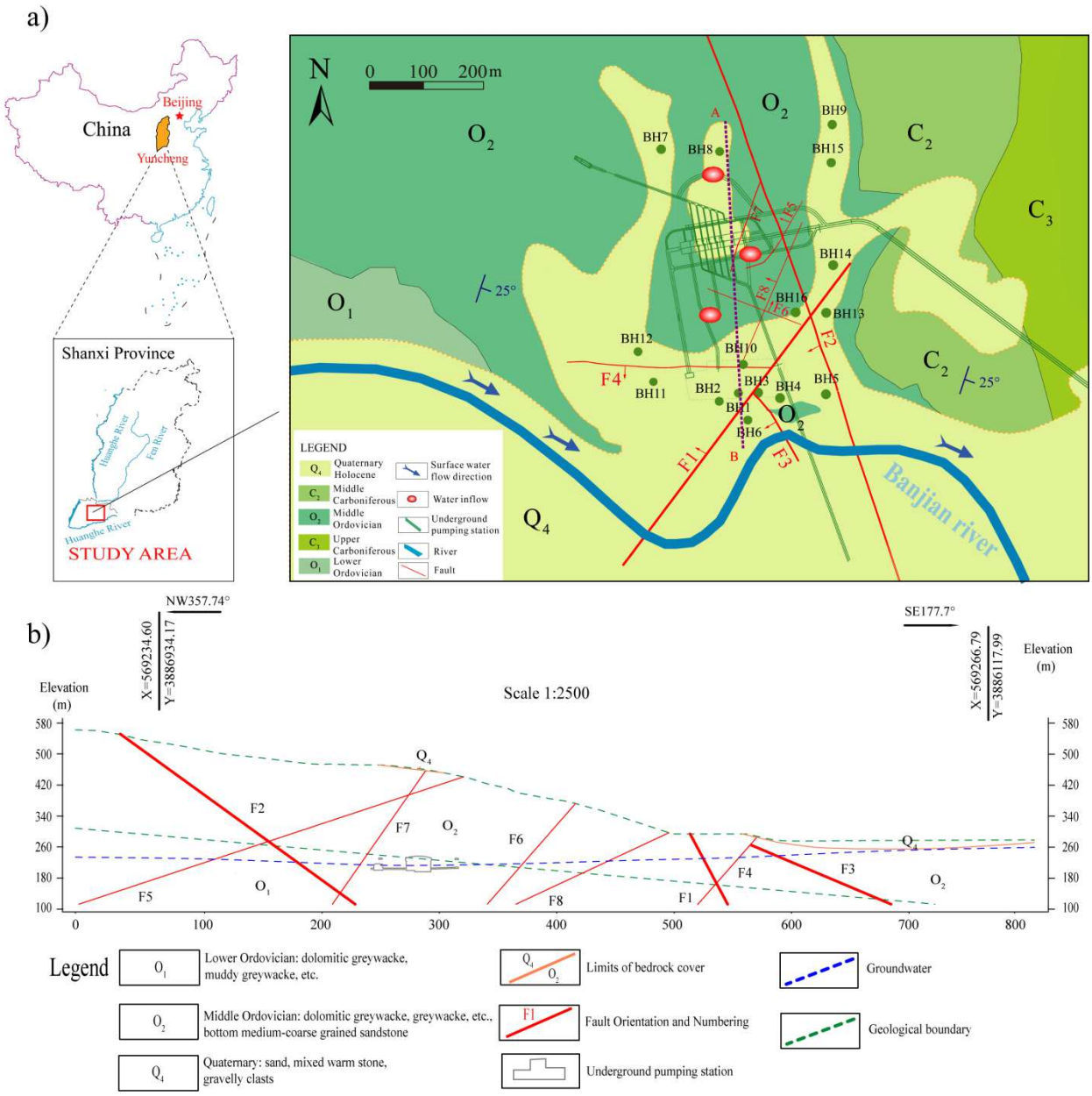


Fig. 1 a) Simplified hydrogeological map of the study area and b) geologic cross-section of the study area basin corresponding to A-B in Fig. 1a.

Surface mapping and underground excavation in the study area have revealed eight faults, among which the larger-scale F1, F2, and F3 faults exhibit varying degrees of seepage in their exposed sections within the cavern (Fig. 1b).

The water inflow in the underground pumping station of the study area is primarily concentrated at three locations within the cavern, with minor seepage observed in the remaining sections. A drainage channel system was constructed on-site to collect and discharge the inflow from various points, while daily flow monitoring was conducted. The monitored daily inflow rates at the pumping station from September 2021 to November 2023 are presented in Fig. 2. The data indicate that during the initial period, inflow increased significantly and remained elevated due to factors such as extreme weather events and upstream reservoir releases. Subsequently, the inflow exhibited notable fluctuations and a declining trend. These observations suggest that the dynamics of water inflow in the study area exhibit

significant nonlinear and nonstationary behavior.

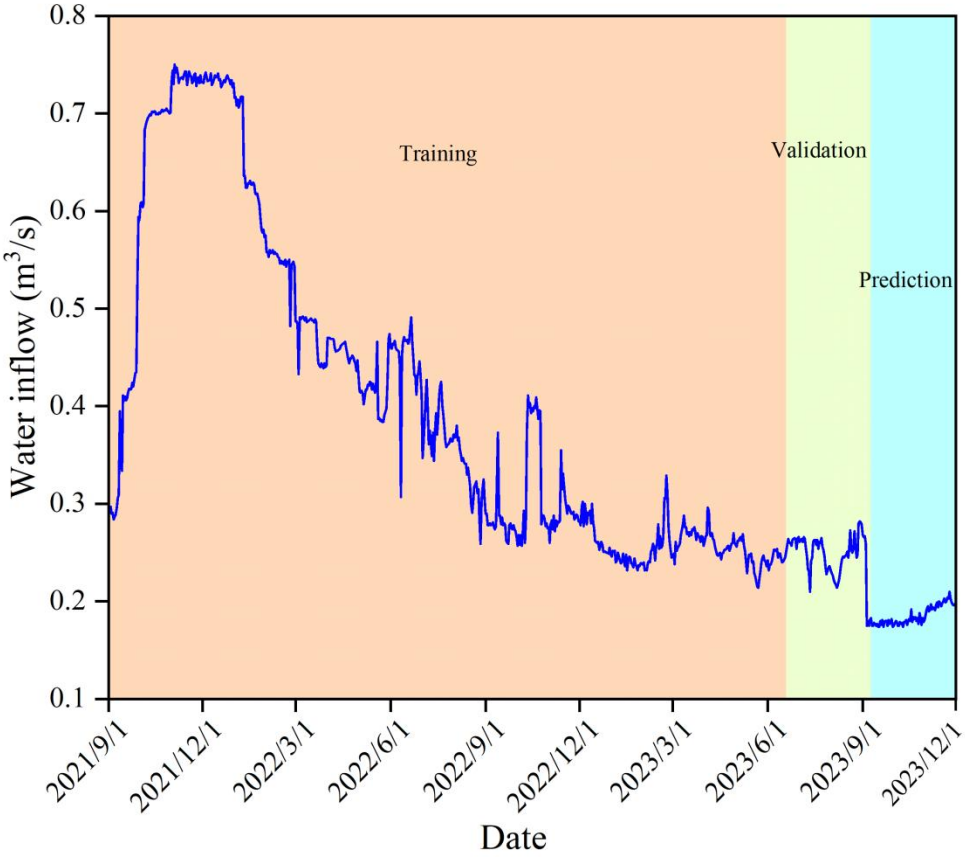


Fig. 2 Daily Water inflow in the study area (September 1, 2021, to November 30, 2023).

3. Method

3.1 Mechanism of water inflow

3.1.1. Rock permeability

Analysis of the geological and hydrogeological conditions in the pump station area was conducted through an integrated interpretation of multi-source data. The lithological assemblage was first determined from borehole cores, and the attitudes of rock strata were measured and statistically analyzed to examine their spatial-temporal relationships with the underground caverns. Subsequently, rock quality designation (RQD) data from all 16 boreholes along the alignment were compiled and plotted as distribution maps to quantitatively evaluate rock mass integrity. Sections with RQD $\leq$ 10% were specifically defined as severely fractured zones, and their spatial correlation was analyzed in conjunction with geological plan maps. Concurrently, the surrounding rock was classified into structural types based on construction-phase logging records, and the proportion of each category was quantified. Permeability of the rock mass was assessed using Lugeon (Lu) values obtained from in-situ water pressure tests. These values were classified into permeability grades according to the Chinese National Standard Standard for Engineering Classification of Rock Masses (GB/T 50218-2014), thereby characterizing the spatial heterogeneity of permeability [41].

Furthermore, by systematically comparing the spatial distribution, dynamic evolution, and total discharge of water inflow points during the excavation and post-lining periods, the response pattern of groundwater to excavation-induced unloading was analyzed. This information was used to infer the regional fractured aquifer unit's continuity and hydraulic behavior. The above analyses were

synthesized to develop an integrated understanding of the seepage structure within the surrounding rock and its dynamic response to engineering activities.

3.1.2. Karst and structure

The analysis of structural and karst controls on groundwater flow adopted an integrated multi-method approach. First, based on the geometry of gently dipping strata and major steeply dipping faults, the regional groundwater flow pattern was interpreted, and a conceptual three-dimensional water-conducting network was constructed. The role of these faults as primary groundwater conduits was investigated by examining their surface exposures along the Banjian River bank, analyzing the intersection angles between fault strikes and the river channel, and documenting the characteristics of fractured and karstified rock within the fault zones through field mapping and borehole data. Macroscopic karst development intensity and its spatial heterogeneity were assessed by integrating surface geomorphology, the distribution of karst cavities encountered in boreholes, and borehole televiewer logging data. These logging data were specifically used to classify the nature of structural planes and identify dissolution features, thereby distinguishing between fracture-dominated and karst-dominated permeability. The connectivity and hydraulic significance of karst features were evaluated by analyzing their spatial association with major fault zones. Finally, the interaction between the extensively developed fracture network and the discrete high-permeability structural pathways was synthesized to explain the observed mechanisms of groundwater inflow into the caverns.

3.2. Prediction of water inflow

Fig. 3 shows the schematic diagrams of the CEEMDAN-LSTM, SA-CEEMDAN-LSTM, and CEEMDAN-LSTM-SA processes.

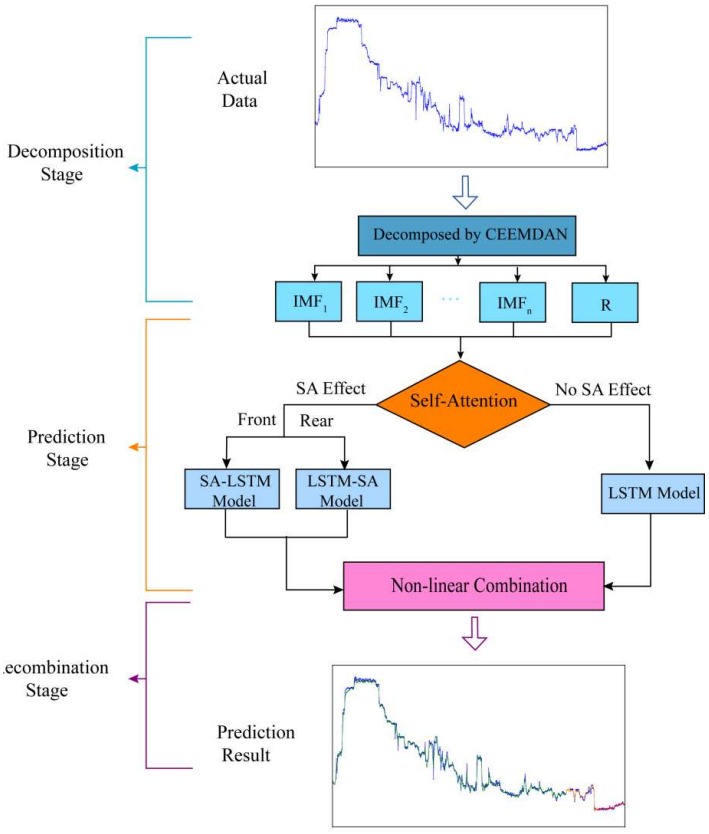


Fig. 3 Schematic diagram of the CEEMDAN-LSTM, SA-CEEMDAN-LSTM, and CEEMDAN-LSTM-SA processes.

3.2.1. CEEMDAN

As a signal decomposition technique developed from Empirical Mode Decomposition (EMD) and its integrated variant, Ensemble EMD (EEMD), CEEMDAN (Complete Ensemble EMD with Adaptive Noise) effectively mitigates mode mixing and misalignment in the final ensemble average caused by inconsistencies among individual intrinsic mode function (IMF) results [42, 43]. It also significantly reduces reconstruction error and computational cost. Compared to other steady-state decomposition methods, CEEMDAN offers several distinct advantages:

(1) Unlike EEMD, which relies on repeated averaging of added Gaussian white noise, CEEMDAN introduces an adaptive noise mechanism that resolves the mode mixing problem inherent in EMD while achieving negligible reconstruction error.

(2) It dynamically adapts to local signal characteristics based on fluctuations and frequencies, allowing for more accurate extraction of IMFs from the original water inflow output sequence and improving the robustness and accuracy of the decomposition.

(3) The integrated averaging process substantially reduces variability across IMF results, ensuring consistency in the ensemble average.

Therefore, this study uses CEEMDAN to decompose the water-inflow output power data. The specific procedure is outlined below:

① Adaptive white noise is added to the original water inflow signal *x(t),* with its amplitude dynamically adjusted based on short-term output fluctuations. The first IMF is then obtained by averaging the corresponding decompositions.

$$\mathrm{IMF}_1=\frac{1}{N}\sum_{i=1}^{N} E_1\left(x(t)+\varepsilon_0 n_i(t)\right) \tag{1}$$

② The first residual component $r_1(t)$ is calculated as follows:

$$r_1(\mathrm{t})=x(\mathrm{t})\text{-}\mathrm{IMF}_1 \tag{2}$$

③ A new signal is constructed by combining $r_1(t)$ with a new adaptive noise sequence. This signal is decomposed via EMD to obtain the second IMF (which is identified as the third IMF in the complete CEEMDAN sequence).

$$x_1(t)=r_1(\mathrm{t})+\mathrm{E}_1\left(n_i(t)\right) \tag{3}$$

$$\mathrm{IMF}_2=\frac{1}{N}\sum_{i=1}^{N} r_1(t)+\mathrm{E}_1\left(n_i(t)\right) \tag{4}$$

④ Step 3 is repeated iteratively to obtain the n-th residual signal $r_n(\mathrm{t})$ and the subsequent $(n+1)$-th IMF.

$$r_n(t)=r_{n\text{-}1}(t)\text{-}\mathrm{IMF}_\mathrm{n}(\mathrm{t}) \tag{5}$$

$$\mathrm{IMF}_{n+1}=\frac{1}{\mathrm{N}}\sum_{i=1}^{N} E_1(r_n(t)+E_n\left(n_i(t)\right)) \tag{6}$$

⑤ The process continues until the residual contains no meaningful oscillatory components, at which point the original signal *x(t)* can be reconstructed as the sum of all extracted IMFs and the final residual:

$$x(t)=\sum_{n=1}^{K}\mathrm{IMF}_\mathrm{n}+r(t) \tag{7}$$

As an enhanced version of EEMD, CEEMDAN overcomes its key limitations—such as reconstruction error, computational inefficiency, and residual noise—thereby achieving superior performance in mode separation and decomposition accuracy [44].

In signal processing and hydrological time series analysis, the energy of an IMF component is typically quantified by the sum of squared amplitudes. For each extracted component, IMFi, its total

energy E_i is defined as the sum of the squares of all values in the sequence over time:

$$E_i = \sum_{t=1}^{N} IMF_i(t)^2 \quad (8)$$

where N denotes the total number of sampling points; this study performed energy calculations using a subset of samples (N=247) encompassing groundwater discharge processes during both extreme weather events and the stable lining period, and t represents the timestep index.

The energy proportion Pi quantifies the contribution rate of the corresponding physical mechanism to the overall groundwater discharge fluctuations:

$$P_i = \frac{E_i}{\sum E_{IMF} + E_R} \times 100\% \quad (9)$$

where E_R denotes the energy of the residual term.

3.2.2. LSTM

Traditional RNNs often struggle with long sequences due to the exponential growth or decay of gradients during backpropagation, hindering their ability to learn long-term dependencies. LSTM networks address this issue by introducing gated mechanisms and a cell state [45, 46].

As a specialized type of recurrent neural network, LSTM—like other neural networks—consists of an input layer, one or more hidden layers, and an output layer. The neurons in its hidden layer can receive information not only from the input layer but also from the perceived information of neurons at the previous time step. This recurrent structure (Fig. 4a) enables RNNs to capture intrinsic features in time-series data. However, recurrent neural networks (RNNs) suffer from the vanishing gradient problem, which makes it difficult for such models to learn long-range causal relationships over extended time periods [47]. To overcome this limitation, Hochreiter and Schmidhuber [48] proposed replacing the standard cell units in RNNs with "memory blocks". This modification significantly enhances the network's ability to retain long-term dependencies, hence the name Long Short-Term Memory network.

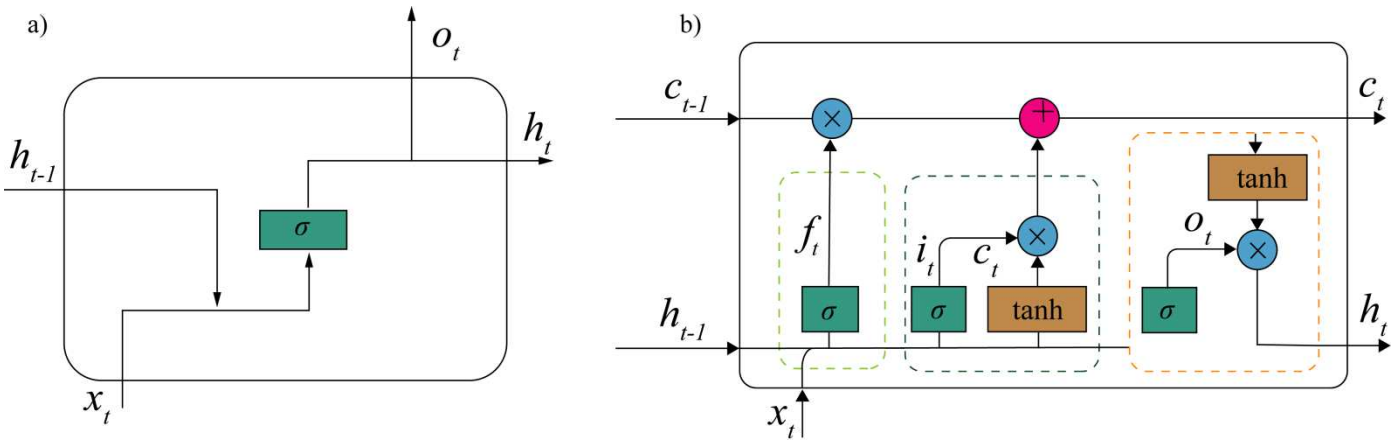


Fig. 4 a) RNN model structure and b) LSTM model structure.

Fig. 4b illustrates the typical structure of an LSTM memory unit. At time step t, the inputs to the memory unit include the hidden state variable h_{t-1} from the previous time step, the cell state variable c_{t-1}, and the current input x_t. The model then sequentially processes these through three gating mechanisms—the forget gate f_t, the input gate i_t, and the output gate otot—to obtain the hidden state h_t and cell state c_t at time t. Finally, h_t is passed to the output layer to generate the LSTM's result y_t at the current step, while both h_t and c_t are propagated to the next time step. The detailed procedure is as follows [33].

During computation at time t, the first step is to compute the forget gate f_t, which determines how

much information from the previous cell state to discard. The formula for f_t is given by:

$$f_t=\sigma\left(U_f x_t+W_f \mathrm{h}_{t-1}+b_f\right) \tag{10}$$

Where U_f, W_f, and b_f denote the adjustable parameter matrices or vector of the forget gate, which are optimized during neural network training; and σ represents the Sigmoid activation function, whose calculation formula is as follows:

$$\sigma(x)=\frac{1}{1+e^{-x}} \tag{11}$$

Where U_i, W_i, and b_i are the adjustable parameter matrices or vectors for the input gate, which are optimized during the neural network training process. The calculation formula for the newly acquired information i_t is as follows:

$$i_t=\sigma(U_i x_t+W_i \mathrm{h}_{t-1}+b_i) \tag{12}$$

Where U_i, W_i, and b_i are the adjustable parameter matrices or vectors for the input gate, which are optimized during the neural network training process. The calculation formula for the newly acquired information $\mathrm{c_t}'$ is as follows:

$$c_t'=\tan \mathrm{h}(U_c x_t+W_c \mathrm{h}_{t-1}+b_c) \tag{13}$$

Where U_c, W_c, and b_c are the adjustable weight matrices and bias vector for c_t', all of which are optimized during neural network training; and tan$h$ denotes the hyperbolic tangent activation function:

$$\tan \mathrm{h}(x)=\frac{e^{x}-e^{-x}}{e^{x}+e^{-x}} \tag{14}$$

Next, the neuron state is updated using the results calculated above, as expressed in the following formula:

$$c_t=f_t \odot c_{t-1}+i_t \odot c_t' \tag{15}$$

Where the symbol $\odot$ denotes the Hadamard product (element-wise multiplication of matrices).

The cell state variable c_t' is key to LSTM's ability to maintain long-term memory. Due to its simple linear interactions with other LSTM cell states, information can be preserved with minimal change over extended periods, thereby enabling the LSTM model to mitigate the vanishing or exploding gradient problem during network training.

Then, the output gate o_t is computed. The output gate determines how much information is used to generate the hidden state variable ht at the current time step t. Its calculation formula is as follows:

$$o_t=\sigma(U_o x_t+W_o \mathrm{h}_{t-1}+b_o) \tag{16}$$

$$\mathrm{h}_t=o_t \odot \tan \mathrm{h}(c_t) \tag{17}$$

Where U_o, W_o, and b_o are the adjustable parameter matrices and vector for the output gate, all of which are optimized during the neural network training process.

Finally, h_t is passed to the output layer to produce the LSTM's final output, yt, at time step t.

$$y_t=W_d \mathrm{h}_t+b_d \tag{18}$$

Where W_d and b_d are the adjustable parameter matrices and vector for the output layer, all of which are optimized during the neural network training process.

3.2.3. Self-attention mechanism

The attention mechanism was first introduced in 2014 and has since been widely applied in fields such as machine translation and natural language processing. In this mechanism, computations primarily rely on an encoder-decoder architecture, which hinders efficient parallel processing. To overcome this limitation, researchers developed the Transformer model, which uses a self-attention mechanism. Both the encoder and decoder in the Transformer employ self-attention layers, significantly improving the efficiency and accuracy of machine translation. The self-attention layer

projects the input sequence onto three trainable matrices — W_q, W_k, and W_v — to generate Query, Key, and Value vectors, respectively (Fig. 5). This design enables effective capture of long-range dependencies within the sequence. It facilitates the extraction of deep-level features [49, 50].

The core of self-attention lies in computing attention scores that capture correlations between vectors within the time series. Specifically, each score indicates the degree of attention that a vector at one time step pays to other vectors in the input sequence. This can be expressed as score(q_i, k_j), where i and j denote the i-th and j-th time steps, respectively ($0 \le i, j \le L$), with L being the total number of time steps, q_i representing the query vector at the i-th time step, and $k_j$representing the key vector at the j-th time step.

To enhance computational efficiency, the L query vectors are typically packed into a matrix $Q = [q_1, q_2, \ldots, q_L]^T$, while the key and value vectors are similarly organized into matrices $K = [k_1, k_2, \ldots, k_L]^T$ and $V = [v_1, v_2, \ldots, v_L]^T$, respectively. In specific simplified model designs, the key matrix K is set equal to the value matrix V to reduce complexity.

The attention score, score (Q, K), can generally be computed using three types of attention functions: additive attention, dot-product attention, and scaled dot-product attention.

Among these, the scaled dot-product attention is widely adopted in practice due to its computational efficiency and effectiveness in stabilizing gradients during training.

$$score(Q,K)=\begin{cases} V^T \tanh(W\cdot Q+U\cdot K), & additive\ \ attention \\ \dfrac{Q\cdot K^T}{\sqrt{d_k}}, & scaled\ \ dot-product\ \ attention \\ Q\cdot K^2, & dot-product\ \ attention \end{cases} \tag{19}$$

Where W denotes the weight matrix between the input layer and the hidden layer, U represents the weight matrix between the hidden layers, and d_k is the scaling factor.

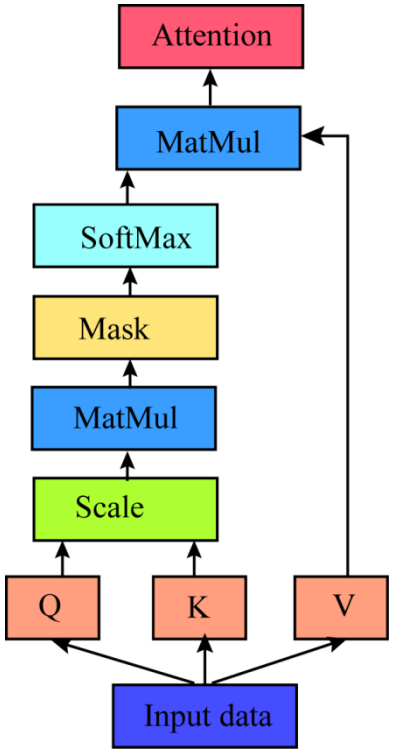


Fig. 5 Self-Attention mechanism structure.

3.2.4. Construction and comparison of fusion models.

This study proposes an interpretable hybrid deep learning model, CEEMDAN-LSTM-SA, to

address the challenge of water inflow prediction in karst systems with scarce data. The model integrates the strengths of CEEMDAN, LSTM, and SA mechanism. To further explore the effectiveness of the SA mechanism and its optimal integration strategy, three model architectures are constructed and systematically compared, allowing for a systematic analysis of the distinct roles of SA.

- **Model I: CEEMDAN-LSTM (baseline model)**

The CEEMDAN-LSTM model serves as the baseline in this study, and its architecture follows the classic "decomposition-forecasting-ensemble" paradigm. First, the model employs the CEEMDAN algorithm to adaptively decompose the original non-stationary time series data into a set of relatively stable IMFs and a residual (Res) component. Subsequently, an independent LSTM submodel is constructed for each resulting component to enable parallel temporal learning and forecasting. Finally, the predictions from all components are summed linearly to reconstruct the final forecast for the original sequence. This model deliberately avoids complex feature- or result-reweighting mechanisms. Its core design objective is to validate the LSTM model's fundamental capability to capture the temporal patterns of individual components after CEEMDAN preprocessing, thereby establishing a clear performance benchmark for enhanced models that incorporate the Self-attention mechanism in subsequent analyses.

- **Model II: CEEMDAN-SA-LSTM**

Fig. 7 illustrates the architectures of the CEEMDAN-SA-LSTM and CEEMDAN-LSTM-SA models, respectively. Their overall framework consists of four core modules: a CEEMDAN decomposition layer, a self-attention (SA) layer, an LSTM network layer, and several fully connected layers.

The key distinction between the two models lies in the order of information processing. In the CEEMDAN-SA-LSTM model (Fig. 6a), the self-attention mechanism precedes the LSTM layer. Its workflow is as follows: first, adaptive decomposition and feature reorganization are applied to the original sequence; subsequently, the self-attention layer assesses the global importance of features and assigns corresponding weights; finally, the LSTM layer processes the weighted sequence to capture temporal dependencies and generate predictions. This pre-LSTM self-attention design allows the model to focus on critical features before sequence modeling, resulting in superior performance compared to a standalone LSTM model in capturing long-range dependencies, resisting noise interference, and enhancing model interpretability.

- **Model III: CEEMDAN-LSTM-SA**

In the CEEMDAN-LSTM-SA model (Fig. 6b), the self-attention mechanism is placed after the LSTM layer. Its workflow proceeds as follows: the decomposed modal components are first processed independently by the LSTM layer to extract temporal features; then, the self-attention layer integrates the outputs from all LSTMs, capturing intrinsic relationships among different components; finally, the data passes through a Dropout layer and an output layer to yield the prediction results. This post-LSTM self-attention design offers two main advantages: first, it avoids potential bias in feature weighting that can arise when self-attention is applied too early without sufficient sequential context; second, it compensates for the limitations of a single LSTM in capturing long-range dependencies within lengthy sequences. Consequently, this architecture not only comprehensively extracts hidden features from the data but also effectively enhances the modeling of sequence correlations, thereby demonstrating significant advantages in prediction accuracy, noise resistance, and interpretability of decision-making.

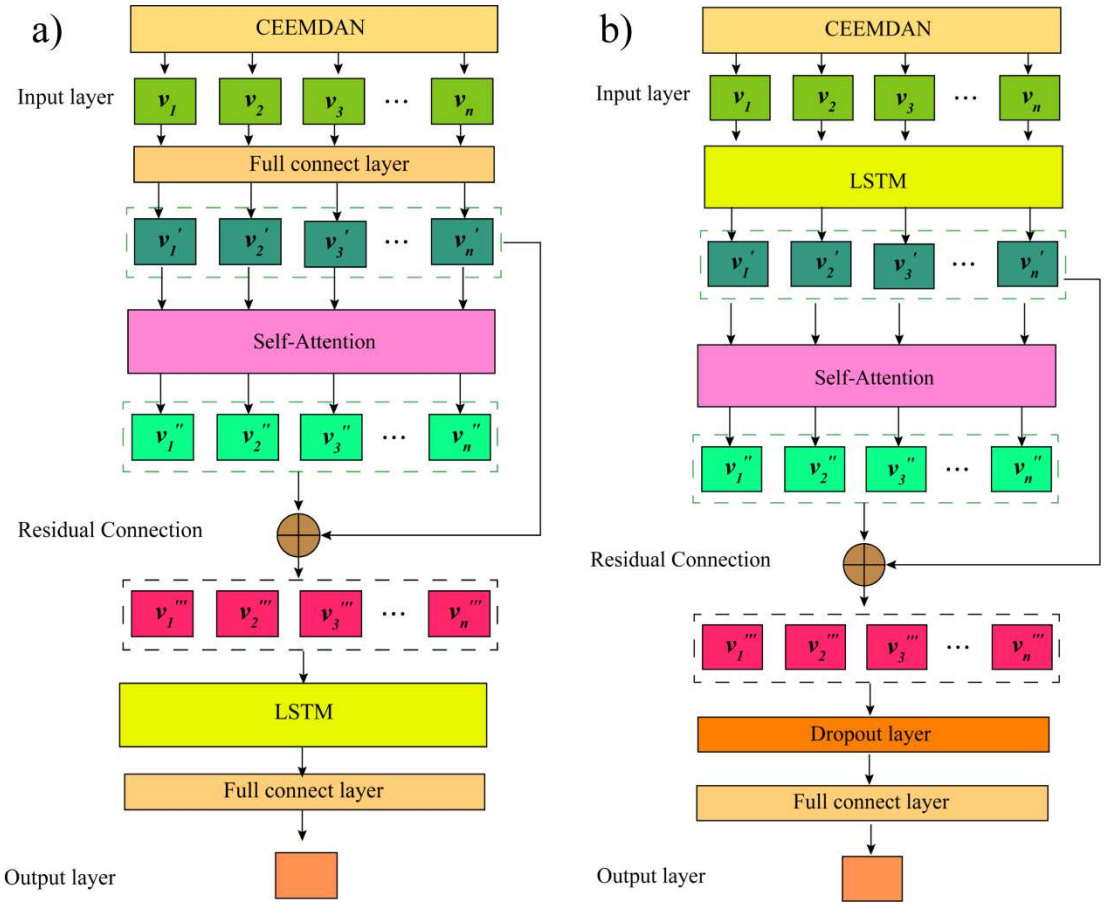


Fig. 6 a) CEEMDAN-SA-LSTM and b) CEEMDAN-LSTM-SA structure diagram.

3.2.5. Model Evaluation Metrics

To further validate the models' predictive accuracy, four evaluation metrics—Root Mean Square Error (RMSE), Mean Absolute Error (MAE), Mean Absolute Percentage Error (MAPE), and R2—are used to assess each model's performance. Among these, RMSE imposes a higher penalty on larger errors, making it suitable for scenarios sensitive to error magnitude. MAE measures the average absolute deviation between predicted and actual values and is appropriate when errors are relatively symmetric. MAPE expresses the prediction error as a percentage, reflecting the relative magnitude of deviation. Additionally, when using the R^2 value to compare the relationship between actual and predicted values, a high R^2 indicates good predictive performance [51]. The formulas for these metrics are defined as follows:

$$MSE(y,\hat{y}) = \frac{1}{n}\sum_{t=1}^{n}(y_t - \hat{y})^2 \tag{18}$$

$$RMSE(y,\hat{y}) = \sqrt{\frac{1}{n}\sum_{t=1}^{n}(y_t - \hat{y})^2} \tag{19}$$

$$MAE(y,\hat{y}) = \frac{1}{n}\sum_{t=1}^{n}|y_t - \hat{y}_t| \tag{20}$$

$$MAPE(y,\hat{y})=\frac{100\%}{n}\sum_{t=1}^{n}\left|\frac{y_t-\hat{y}_t}{y_t}\right| \tag{21}$$

$$R^2=1-\frac{\sum_{i=1}^{M}(y_t-\hat{y}_t)^2}{\sum_{i=1}^{M}(y_t-\bar{y}_t^2)} \tag{22}$$

Where y_t represents the actual value, $\hat{y}_t$ enotes the predicted value, $\bar{y}$ indicates the mean value, and n is the number of time steps.

Generally, smaller values of MSE, RMSE, MAE, and MAPE indicate more accurate model predictions, while an R^2 value closer to 1 reflects a better model fit.

4. Results and discussion

4.1. Analysis of the mechanism of water inflow

4.1.1. Rock permeability

The underground pumping station is situated in rock formations dominated by Ordovician limestone and dolomitic limestone, interbedded with marl and shale. This alternating sequence of hard and soft strata provides the material basis for structural fragmentation. Core logging reveals extremely poor physical integrity of the rock mass, with fracture surfaces commonly exhibiting iron oxide staining and clay-filled materials, indicating long-term tectonic disturbances and water-rock interactions (Fig. 7).



BH3 Box 6, 22.2–26m

BH7 box 5, 17.4-21.3m

BH16 box 5, 148-152.8m

Fig. 7 Observations from representative drill cores.

Spatial statistics of the RQD show that the rock integrity across the entire area is at an exceedingly low level (RQD < 50%) (Fig. 8). Particularly within fault-influenced zones, RQD values frequently drop below 10% or even reach zero. This extremely low RQD distribution not only confirms the high proportion (90%) of Class IV–V surrounding rock (Table 1) but also structurally indicates that the rock mass possesses the conditions to transition from a "fractured medium" to a "shattered-fragmented or loose medium." The permeability coefficient of the surrounding rock exhibits significant variations,

ranging from 5–20 Lu (moderate permeability) to 50–80 Lu (locally high permeability), quantitatively characterizing its pronounced spatial heterogeneity.

Table 1 Statistical Table of Surrounding Rock Types for the Main Caverns in the Underground Pump Station Area

Surrounding rock type	Cavern name	Distribution length in tunnel (m)	Percentage within tunnel/cavern (%)	Percentage within underground pump station area (%)
V	Ventilation tunnel no. 1	156	64.5	59.2
	Access adit no. 1, section 3	61	52.6	
	Access adit no. 1, section 1	30	14.6	
	Access tunnel no. 1	979.3	88.8	
	Access tunnel no. 2	120.5	69.7	
	Access adit no. 4	192	100	
	Lower drainage gallery	60	20	
	Penstock	172	74.5	
IV	Ventilation tunnel no. 1	85.8	35.5	28.8
	Upper drainage gallery, section I	247.4	100	
	Access tunnel no. 1	114.1	10.3	
	Access tunnel no. 2	28	16.2	
	Discharge valve chamber	88.3	100	
	Lower drainage gallery	240	80	
	Penstock	59	25.5	
III	Access adit no. 1, section 3	55	47.4	12
	Upper drainage gallery, section II	70.6	100	
	Upper drainage gallery, section III	21.4	100	
	Access adit no. 1, sections I & II	175.6	85.4	
	Access tunnel no. 1	10	0.9	
	Access tunnel no. 2	24.5	14.1	

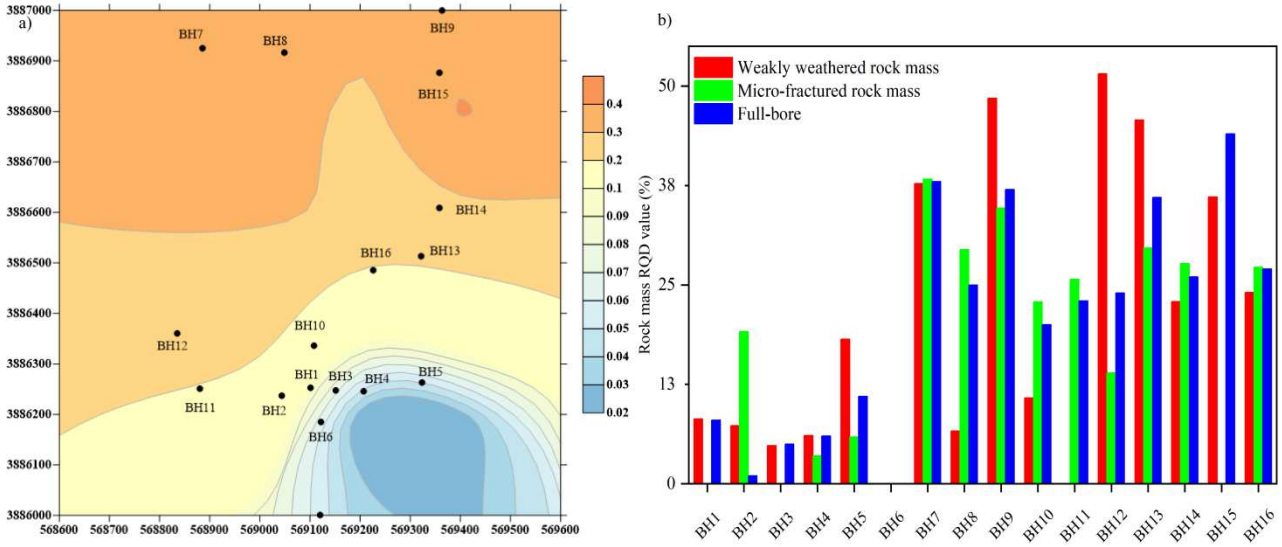


Fig. 8 a) Full-bore RQD contour cloud map and b) Statistical results of RQD from regional borehole cores.

The evolution of water seepage during tunnel advancement provides a clear view of the aquifer's dynamic nature. The dynamic displacement and widespread distribution of seepage points, which shift progressively as the tunnel face advances, confirm the presence of a highly interconnected fracture network within the rock mass. Moreover, the instantaneous unloading induced by excavation triggers secondary fracturing, rendering groundwater highly sensitive to the reconstruction of pressure gradients. This results in a pronounced forward-shift effect of the depressurization cone (Fig. 9).

After lining completion, seepage points became markedly concentrated, with the total seepage volume not decreasing despite the reduced discharge area. This indicates the presence of a cross-scale quasi-continuous fractured aquifer unit surrounding the tunnel. The introduction of the lining structure merely altered the groundwater boundary conditions, transitioning it from the initial "extensive, unconfined diffuse seepage" to "confined, pressurized seepage" (Fig. 9).

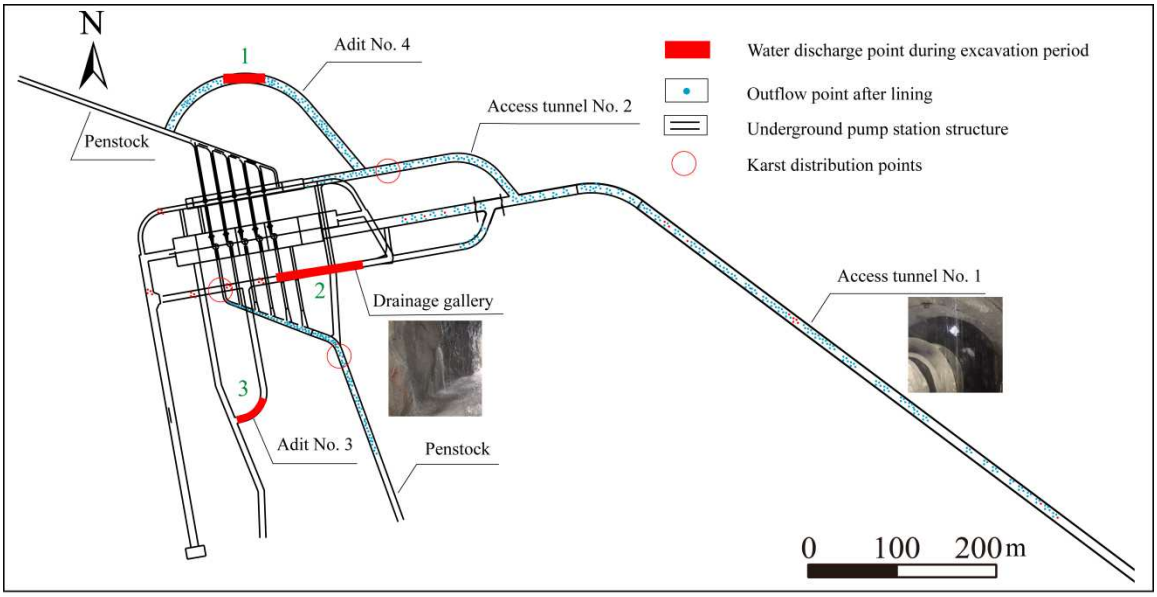


Fig. 9 Distribution of water outlets during the excavation and lining periods of the underground pumping station.

As regional groundwater flow continuously replenishes the tunnel periphery through the fracture network, pore water pressure behind the lining progressively accumulates. Once a critical threshold is reached, groundwater eventually breaches structural weaknesses or tectonic planes, completing a nonlinear transition in discharge mode from "distributed flow" to "pipeline flow." This localized, concentrated pipe-flow phenomenon robustly confirms that the surrounding rock aquifer has strong hydraulic replenishment capacity and exhibits pronounced regional hydraulic equilibrium.

4.1.2. Karst and tectonics

The groundwater flow system in the study area is strongly controlled by tectonics. A three-dimensional conduit topological network, formed by the spatial interconnection of gently dipping bedding planes and steeply dipping fault systems (F1, F2, F3), facilitates efficient hydraulic connectivity across different strata. Research confirms that regional groundwater flow directions are highly consistent with tectonic trends. In particular, the F1 and F2 faults, serving as the structural framework's backbone, function as "hydraulic corridors." Through their high-angle intersection with river channels, they promote lateral infiltration of surface water and drive directional groundwater migration along the fault zones [6].

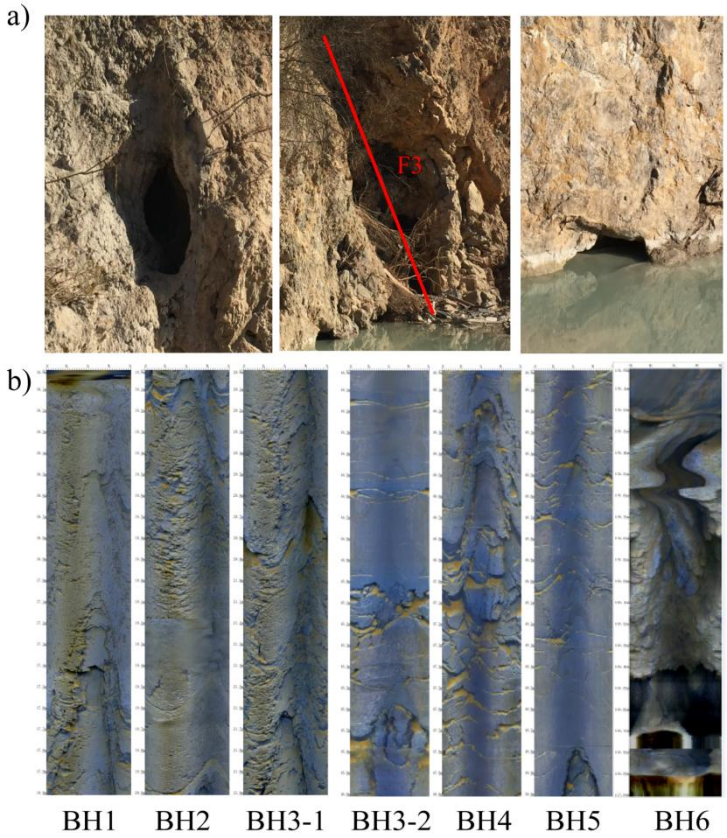


Fig. 10 a) Exposure of fault F3 and its adjacent karst caves and b) borehole teleview log showing karst features.

Karst dynamics within the fault zones further enhance this channelization characteristic. Due to the long-term coupling of intense flow field scour and chemical dissolution, the F3 fault and its influenced zone have evolved into highly permeable discrete conduit channels (Fig. 10a). In contrast, the extensively developed gently dipping bedding fractures form a complementary distributed seepage network, which constitutes the physical basis for the "multi-point dispersed seepage" observed during the excavation period. The most direct validation comes from the significant and sustained concentrated seepage and inflow observed at the exposed points of the F1 and F2 faults within the

underground pumping station. This not only confirms the high connectivity of the internal network within the tectonic-karst system but also reveals its role as a regional water-collection center and a main transmission pathway. Driven by pressure gradients, it facilitates rapid recharge from deeper aquifers towards the low-potential excavated space.

Macro-scale analysis indicates that karst development in the study area is generally at a weak and highly heterogeneous early stage. Aside from locally exposed dissolution cavities approximately 2 meters high within the F3 fault zone, most areas are dominated by sealed dipping fractures and gently dipping bedding planes. Dissolution features are rare, spatial connectivity is poor, and no conduit-type flow paths have formed. Borehole televiewer logging confirms that approximately half of the dissolution traces are strictly developed along fault corridors, revealing that the direct contribution of dissolution to the flow field is limited (Fig. 10b). Essentially, it acts only as a secondary modifying factor controlled by the pre-existing tectonic framework and does not alter the overall hydrogeological character of the rock mass, which remains dominated by fracture flow.

4.1.3. Comprehensive analysis of water inflow mechanisms

In summary, the large-scale water inflow process in the deep underground pumping station can be conceptualized as a typical multi-physical, hydromechanical (HM)- coupled feedback mechanism. This process is fundamentally governed by the nonlinear interaction between the stress redistribution induced by large-scale excavation and the highly heterogeneous, anisotropic fractured media.

(1) Structural Foundation: storage and conveyance in a dual medium

The surrounding rock in the study area primarily consists of Class IV–V rock masses with fractured to fragmented structures. Their highly interconnected fracture network serves a dual function: providing distributed storage and enabling dispersive transport. Within this matrix background, a multi-scale, three-dimensional structural network—formed by the interweaving of gently dipping bedding planes and steeply dipping fractures (F1, F2, F3)—acts as a highly permeable skeleton connecting deep aquifers with surface water. This network dominates the macroscopic convergence and long-distance redistribution of groundwater.

(2) Evolutionary Mechanism: nonlinear flow regime transition under engineering intervention

Excavation phase (Stress release and activation): Initial tunnel advancement disrupts the in-situ stress equilibrium. The instantaneous unloading effect induces fracture opening and propagation, thereby "activating" the latent conductive network. During this stage, the system follows a "free drainage pattern," where groundwater primarily manifests as widespread, dispersive seepage from fine fractures into the excavated space.

Operation phase (Boundary constraint and reconfiguration): The subsequent installation of lining structures introduces a low-permeability boundary constraint. This intervention triggers a profound redistribution and accumulation of pore water pressure. It forces a fundamental restructuring of the seepage field, leading to a nonlinear transition in the flow regime. The initial "dispersed matrix seepage" shifts towards "concentrated conduit flow along structural discontinuities," characterized by localized high-velocity gushing at weak points in the lining.

(3) Dynamic calibration: environmental response governed by fracture networks

Although localized karst dissolution at tectonic intersections enhances permeability, mechanism validation indicates that it acts as a secondary modifying factor and does not alter the fracture network-dominated fluid-dynamic regime. While the stability of the lining boundary constrains the system's baseline flow, it remains highly sensitive to transient meteorological forcing, such as extreme precipitation events. This responsiveness underscores the system's strong hydraulic conductivity, which

is effectively channeled through the structural conduits.

4.2. *Prediction of water inflow*

4.2.1. Time-frequency decomposition of water inflow

In this study, the CEEMDAN algorithm was employed to deconstruct the non-stationary water inflow time series. To suppress modal aliasing while ensuring computational stability, the standard deviation of the added white noise was set to 0.05 with an ensemble size of 100. The raw signal was decomposed into six IMFs, spanning from high to low frequencies, and a singular residual component (R) that encapsulates the underlying evolutionary trajectory of the seepage field (Fig. 11). The mathematical integrity of this decomposition was validated through near-perfect signal reconstruction. The residual component, R, exhibits a non-monotonic evolution: a rapid ascent peaking in October 2021—triggered by extreme meteorological forcing—followed by a sustained decline that reflects the hydromechanical stabilization induced by lining completion and targeted engineering interventions.

Energy spectral analysis provides a quantitative bridge between signal characteristics and the earlier genetic mechanism analysis. The results demonstrate that the residual component accounts for 97.41% of the total energy, numerically confirming the transition of the groundwater system from the 'free-relief' drainage mode during the excavation phase to a structurally constrained 'quasi-steady-state' equilibrium. In contrast, although the high-frequency dynamic components (IMF1–IMF3) account for only 0.41% of the total energy, they uniquely isolate the 'pulse-type' recharge signatures of the karst conduit system during extreme rainfall. This extreme energy disparity indicates that while fast-flow events constitute a minor portion of the regional hydraulic regime, they represent the primary source of transient risk within a system otherwise dominated by stable baseflow.

Table 2 Results of energy density calculations.

Component category	Energy value (E_i)	Energy proportion (P_i)	Associated physical mechanism
High-frequency Components (IMF_{1-3})	0.137	0.41%	Extreme weather responses
Low-to-mid frequency components (IMF_{4-6})	0.724	2.18%	Aquifer regulation
Residual component (R)	32.415	97.41%	Aquifer regulation
Total	33.276	100.00%	Overall hydrodynamic response of the pumping-induced groundwater discharge system

Traditional LSTM models often treat such low-energy signals as noise and filter them out. In contrast, this study effectively isolates these components via CEEMDAN decomposition and assigns appropriate computational weights to low-energy yet high-risk features using the self-attention mechanism, thereby achieving accurate prediction of water surge points.

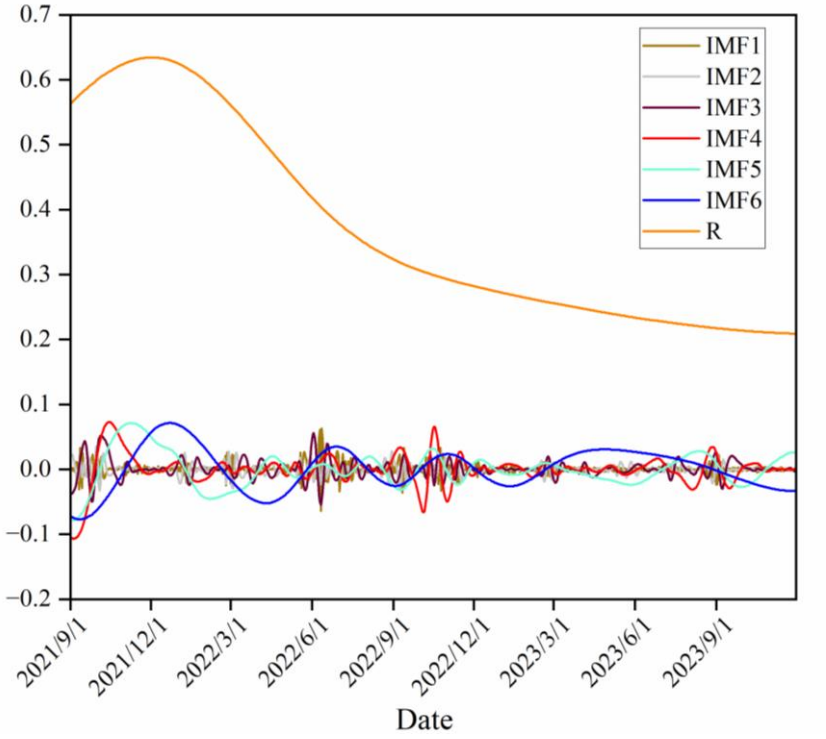


Fig. 11 CEEMDAN decomposition results of Water inflow.

Boxplot analysis revealed distinct differences in the data distribution and central tendency among the IMFs and the residual component, highlighting the heterogeneity of fluctuations across different time scales (Fig.12a). Furthermore, pearson correlation analysis, visualized through a heatmap, indicated generally low absolute correlation coefficients among the components, suggesting weak inter-component relationships (Fig.12b). This result demonstrates the effectiveness of the CEEMDAN decomposition, as the derived components maintain a high degree of independence and successfully extract multi-scale fluctuation information from the water inflow series.

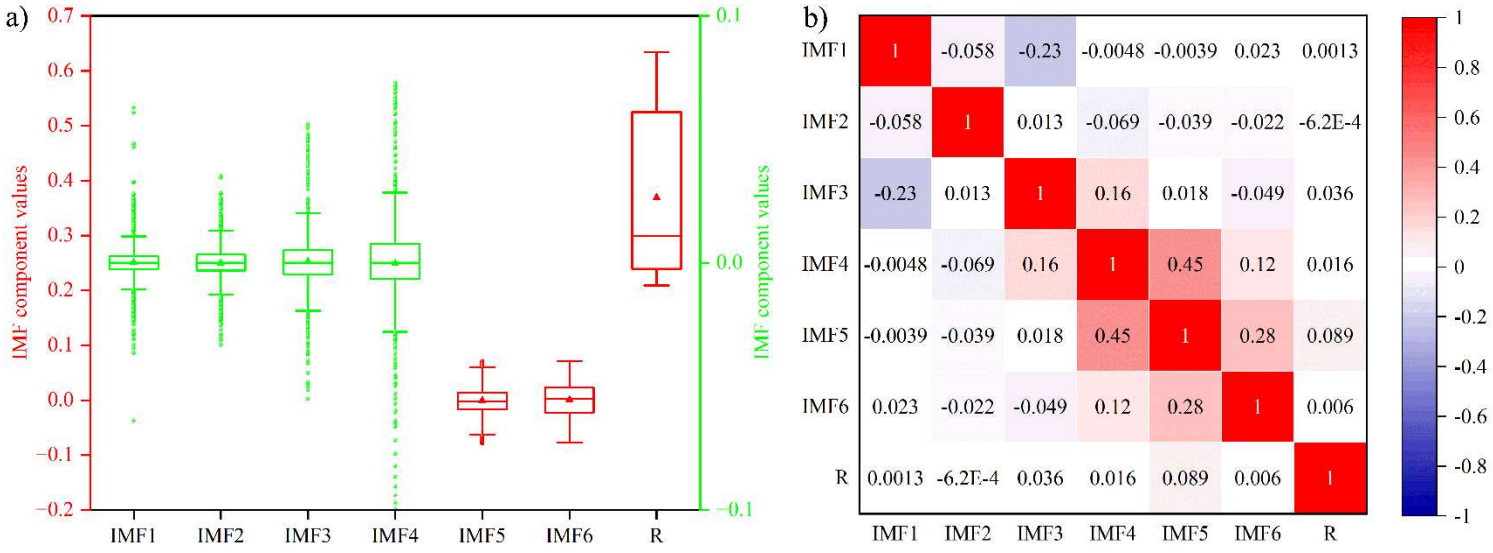


Fig. 12 a) Box plots and b) heatmaps of different water inflow components.

4.2.2. Comparison between CEEMDAN-LSTM, CEEMDAN-SA-LSTM, and CEEMDAN-LSTM-SA

The water inflow time series was divided into three periods: the training period (September 1, 2021, to June 18, 2023), the validation period (June 19, 2023, to September 8, 2023), and the prediction period (September 9, 2023, to November 30, 2023). The training, validation, and prediction sets accounted for 80%, 10%, and 10% of the total water inflow data, respectively. Based on this partitioning, three models were constructed in this study: CEEMDAN-LSTM, CEEMDAN-SA-LSTM, and CEEMDAN-LSTM-SA. In each model, the LSTM, SA-LSTM, and LSTM-SA methods were employed to simulate the individual subsequences, respectively, with the final water inflow reconstruction achieved by integrating the results.

To assess whether the models overfitted during training and validation, this study used training and validation loss curves as diagnostic tools. The loss variations of the three models—CEEMDAN-LSTM, CEEMDAN-SA-LSTM, and CEEMDAN-LSTM-SA, during the respective phases are illustrated in Fig. 13. As shown, both the training loss and validation loss of each model decreased synchronously and eventually converged to a stable plateau. This trend indicates the absence of overfitting and demonstrates that the training process was well-behaved and effective.

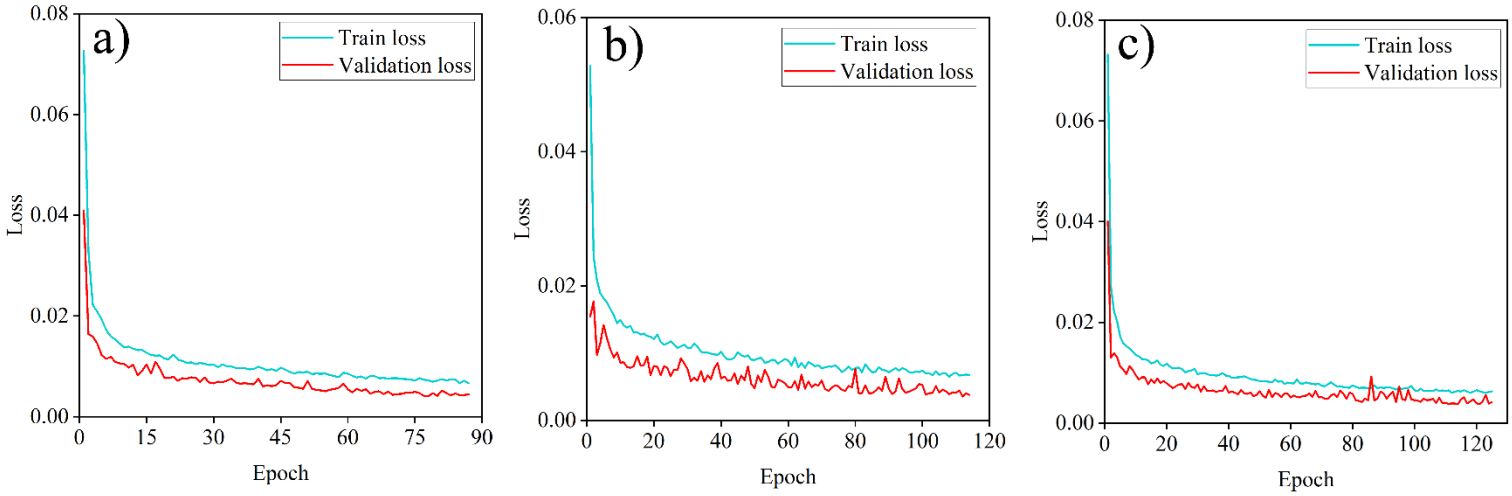


Fig. 13 The loss in the training and validation periods of a) CEEMDAN-LSTM, b) CEEMDAN-SA-LSTM, and c) CEEMDAN-LSTM-SA.

Fig. 14 presents the prediction results of the CEEMDAN-LSTM, CEEMDAN-SA-LSTM, and CEEMDAN-LSTM-SA models for water inflow during the training, validation, and prediction periods, as well as the residual scatter plots for these three periods. Their performance metrics are summarized in Table 3. For the CEEMDAN-LSTM model, the predicted water inflow shows a poor match with the observed values (Fig. 14a). The residual scatter plot is mostly distributed below the zero level (Fig. 14d). Meanwhile, the predictive quality of both the CEEMDAN-SA-LSTM and CEEMDAN-LSTM-SA models surpasses that of the CEEMDAN-LSTM model, with the CEEMDAN-LSTM-SA model achieving the best performance (Fig. 14c and f).

Table 3 Performance metrics of CEEMDAN-LSTM, CEEMDAN-SA-LSTM, and CEEMDAN-LSTM-SA during training, validation, and prediction periods.

Model	Train				Validation				Prediction			
	R2	RMSE	MAE	MAPE	R2	RMSE	MAE	MAPE	R2	RMSE	MAE	MAPE
LSTM	0.994	0.013	0.010	2.514	0.750	0.012	0.009	3.714	0.581	0.006	0.006	3.020
SALSTM	0.995	0.012	0.008	2.033	0.856	0.009	0.007	2.893	0.630	0.006	0.005	2.614
LSTMSA	0.995	0.011	0.007	1.950	0.869	0.009	0.007	2.806	0.902	0.003	0.002	1.254

As shown in Table 1, the R^2 value obtained by the CEEMDAN-LSTM model is lower than that of the CEEMDAN-SA-LSTM and CEEMDAN-LSTM-SA models, indicating that the latter two exhibit superior predictive quality. Meanwhile, the CEEMDAN-LSTM-SA model achieves the highest R^2 value, suggesting that placing the self-attention mechanism after the LSTM layer yields the highest prediction accuracy. Furthermore, during the prediction phase, the CEEMDAN-LSTM-SA model attains the lowest RMSE, MAE, and MAPE, along with the highest R^2, demonstrating that it provides the best predictive performance (Fig. 14c).

Quantitative evaluation further confirms that the CEEMDAN-LSTM model underperforms compared to the CEEMDAN-SA-LSTM and CEEMDAN-LSTM-SA models. Specifically, compared to CEEMDAN-LSTM, the CEEMDAN-SA-LSTM model reduces MAE and MAPE by 16.7% and 13.4%, respectively, while improving R^2 by 7.77%. In contrast, the CEEMDAN-LSTM-SA model further enhances prediction performance, reducing RMSE, MAE, and MAPE by 50%, 66.67%, and 58.48%, respectively, and achieving a 35.35% improvement in R^2 relative to CEEMDAN-LSTM.

Further comparison between the CEEMDAN-SA-LSTM and CEEMDAN-LSTM-SA models shows that the latter achieves additional reductions in RMSE, MAE, and MAPE by 50%, 60%, and 52.03%, respectively, and improves R^2 by 30.16%. Taken together, these metrics indicate that the CEEMDAN-LSTM-SA model delivers the best prediction performance among the three models and validate that positioning the self-attention mechanism after the LSTM layer significantly enhances the prediction accuracy of LSTM-based models.

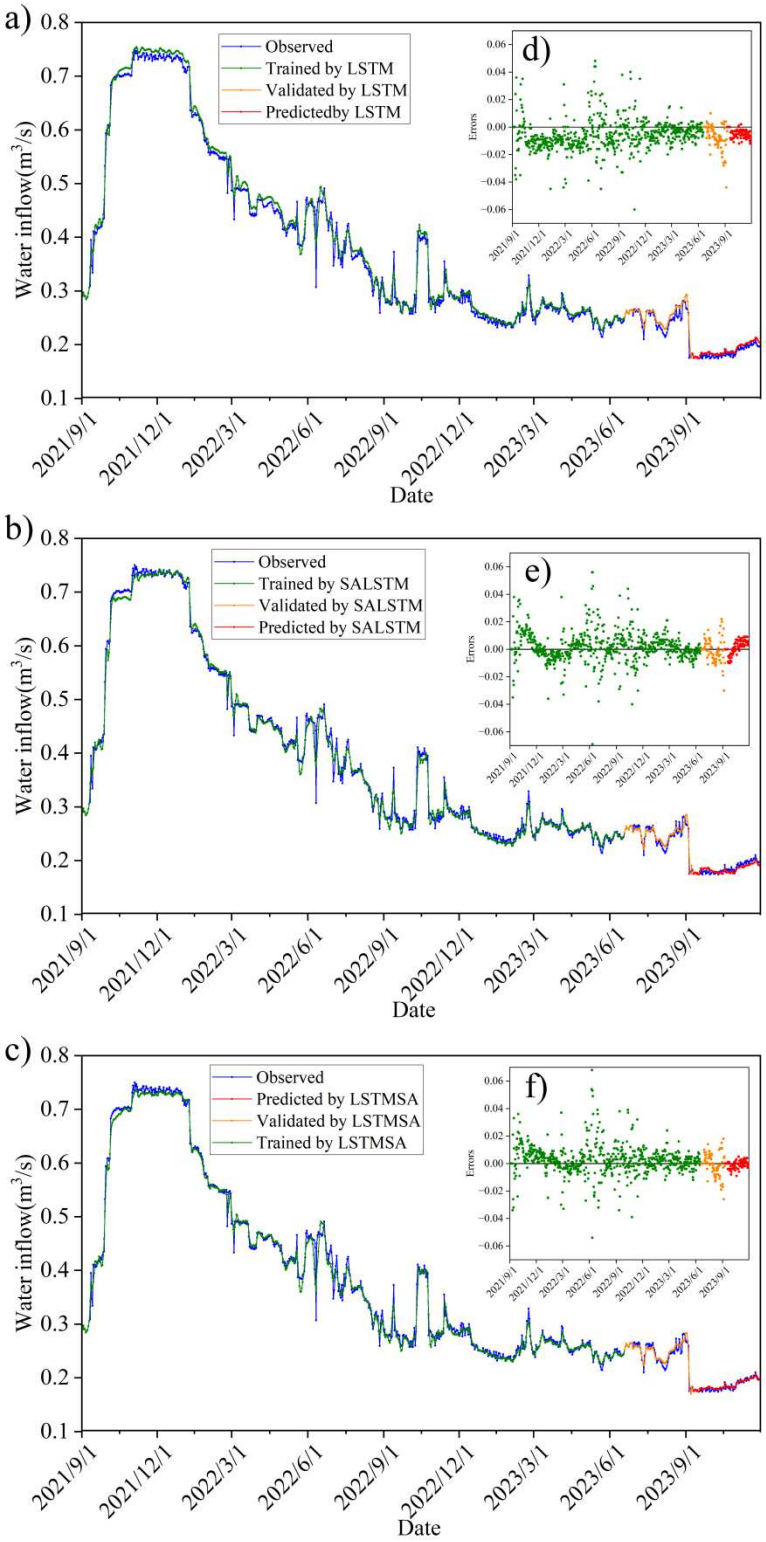


Fig. 14 (a-c) CEEMDAN-LSTM, CEEMDAN-SA-LSTM, and CEEMDAN-LSTM-SA training, validation, and prediction results for water inflow; (d-f) corresponding residual scatter plots of the simulation.

To further explore the predictive ability of different hybrid models, scatter plots of simulated versus observed values for the three models during the training, validation, and prediction periods were also plotted (Fig. 15). The results reveal that both the CEEMDAN-SA-LSTM and CEEMDAN-LSTM-SA models exhibited superior performance compared to the CEEMDAN-LSTM

model, with CEEMDAN-LSTM-SA achieving higher accuracy than CEEMDAN-SA-LSTM. Furthermore, to provide a more in-depth analysis and clarify the reasons for the superior performance of the CEEMDAN-LSTM-SA model compared to the CEEMDAN-SA-LSTM model, Table 4 lists the performance metrics of each component of the CEEMDAN-SA-LSTM and CEEMDAN-LSTM-SA models during the prediction period.

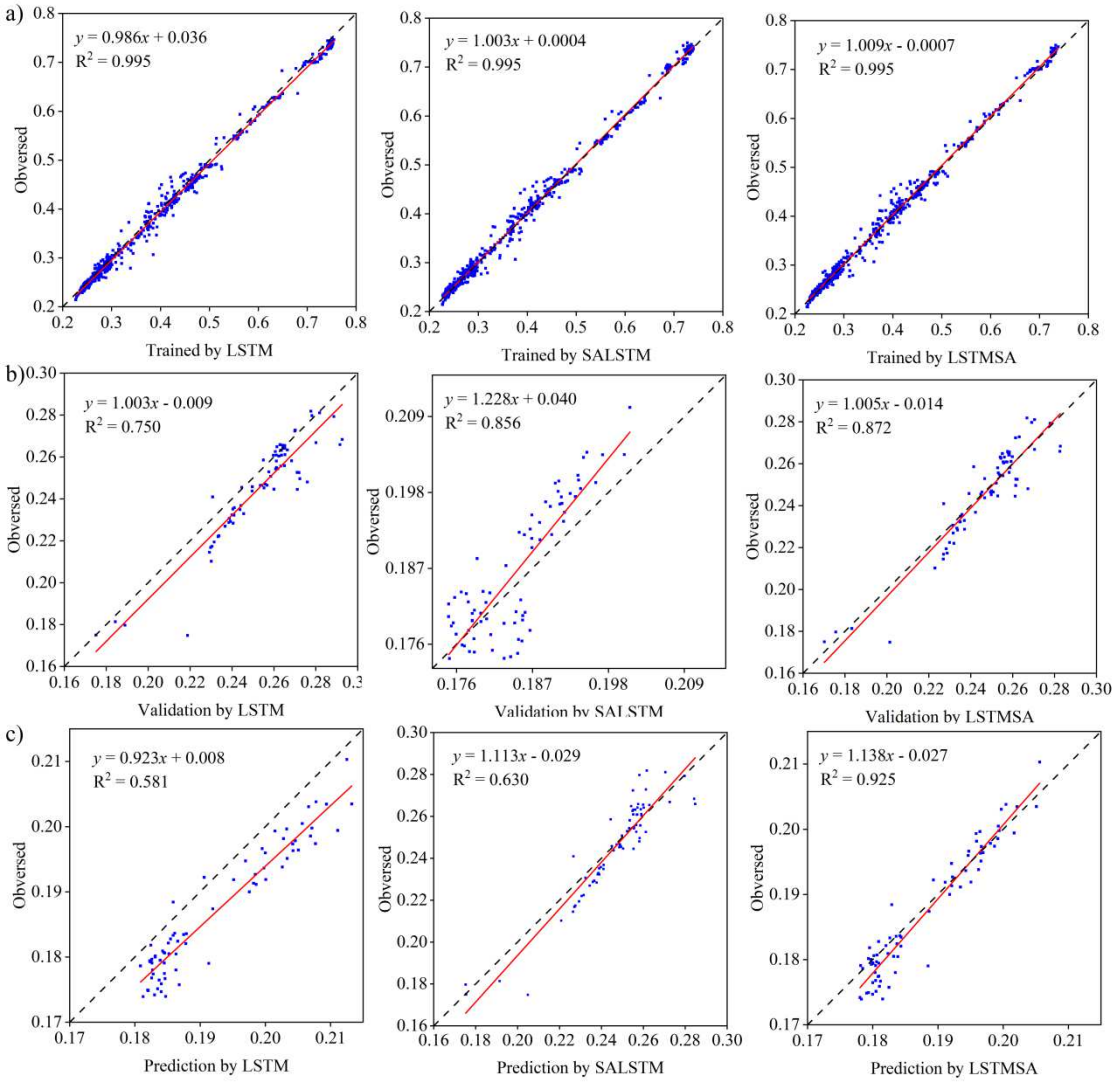


Fig. 15 Scatter plots of simulated versus observed water yield during the a) training, b) validation, and c) prediction periods.

4.2.3. Interpretable analysis

Table 4 presents the refined performance metrics of the proposed CEEMDAN-SA-LSTM and CEEMDAN-LSTM-SA architectures across various IMFs. Overall, both hybrid frameworks demonstrate exceptional fit, with R^2 values exceeding 0.90 and absolute error metrics (RMSE and MAE) consistently near zero (Table 2). This indicates that the models effectively capture the underlying seepage trend, which is dominated by the high-energy residual component.

However, a notable discrepancy emerges in the high-frequency range (IMF1–IMF3): the Mean Absolute Percentage Error (MAPE) shows substantial inflation for both the SA-LSTM (up to 365.7%) and LSTM-SA (up to 550.4%) variants. This localized decline in accuracy is fundamentally linked to the stochastic hydraulic pulses triggered by extreme hydro-meteorological forcing and adjacent

reservoir releases during the September–October 2021 period (Chi et al., 2025). From a signal-processing perspective, these high-frequency components carry the signature of "pulse-type" recharge within the karst aquifer system, characterized by low magnitude but high volatility. The elevated MAPE values are partly attributable to the near-zero baseline of these signals, where even minor absolute deviations can lead to disproportionately high percentage errors.

Physically, the high oscillatory nature of these components reflects the most unpredictable features of the regional groundwater system [17], where nonlinear turbulent flow and rapid conduit flow dominate the hydrological processes—dynamics that standard recurrent units typically fail to capture, as they are better suited for modeling stable baseflow regimes.

Table 4 Performance metrics of CEEMDAN-SA-LSTM and CEEMDAN-LSTM-SA for different Water inflow Components.

IMFS	CEEMDAN-SA-LSTM				CEEMDAN-LSTM-SA			
	R2	RMSE	MAE	MAPE (%)	R2	RMSE	MAE	MAPE (%)
IMF1	0.546	0.003	0.002	105.813	0.656	0.004	0.003	214.041
IMF2	0.805	0.002	0.001	365.764	0.867	0.002	0.002	519.113
IMF3	0.853	0.002	0.002	307.528	0.870	0.002	0.002	550.442
IMF4	0.803	0.003	0.003	820.344	0.966	0.001	0.001	88.631
IMF5	0.968	0.004	0.003	78.642	0.970	0.003	0.003	80.073
IMF6	0.930	0.002	0.003	8.291	0.959	0.001	0.001	6.362
R	0.968	0.003	0.003	1.244	0.984	0.006	0.006	2.894

In contrast, a pronounced structural performance divergence was uniquely observed in the intermediate-frequency component, IMF4. While the SA-LSTM variant exhibited a sharp rise in MAPE to 820.344%, the LSTM-SA architecture maintained a manageable error level of 88.631%, demonstrating its superior ability to decode nonlinear fracture-mediated flow signatures and associated hydrogeological memory effects. Given the dominant energy contribution of the residual and low-frequency components during the post-lining phase, predictive performance on IMF4 serves as a critical benchmark for a model's capacity to extract meaningful physical information from low-energy constituents.

This comparative analysis highlights the advantage of applying self-attention after LSTM processing. The superior performance of the CEEMDAN-LSTM-SA framework over the pre-positioned variant can be attributed to three key signal-processing mechanisms:

(1) Mitigation of Information Decay: Standard LSTMs tend to dilute early-sequence information—a critical limitation when modeling karst aquifers with long-range temporal dependencies. As a global feature recalibrator applied after the LSTM, the self-attention mechanism bypasses this sequential bottleneck, assigning context-aware weights to important historical states and effectively preserving the system's long-term memory.

(2) Enrichment of Temporal Context: When attention is applied before the LSTM, it operates on shallow input features that lack temporal depth, in karst systems, where inflow results from multiple lagged responses, the attention mechanism benefits from the high-level hidden-state representations generated by the LSTM to distinguish between stochastic noise and meaningful pulse signals.

(3) Refinement of Nonlinear Features: By processing LSTM-encoded hidden states—which already embed complex temporal patterns such as nonlinear hydraulic feedback from tunnel lining—the post-positioned self-attention mechanism performs selective focus. It identifies and

emphasizes the most relevant historical activations, yielding more robust and physically consistent outputs even under extreme meteorological forcing.

5. Conclusions

This study establishes a synergistic framework that integrates multi-scale geological mechanism analysis with advanced deep learning to address the challenges of predicting water inflow in deep karst engineering. The principal conclusions are summarized as follows:

(1) Hydromechanical (HM) regime transition: Groundwater ingress is identified as a systematic multi-physical response governed by a robust three-dimensional tectonic network. Engineering boundary shifts fundamentally modulate the evolution of discharge patterns: excavation-induced unloading activates the fractured matrix, resulting in areal seepage, whereas lining installation introduces a low-permeability boundary that triggers pore-pressure redistribution and forces a transition to localized piping. Quantitative energy-spectrum analysis confirms this mechanism numerically, with the residual component accounting for 97.41% of the total signal energy, indicating a structurally constrained quasi-steady-state equilibrium during the post-lining phase.

(2) Mechanism-informed predictive innovation: To overcome the "energy masking effect," in which high-volume background baseflow obscures transient risk signals, the proposed CEEMDAN-LSTM-SA model achieves superior interpretability and precision ($R^2 = 0.902$). By placing the self-attention mechanism after the recurrent layer, the model serves as a global feature recalibrator, enhancing the high-level temporal patterns encoded by the LSTM. This architecture effectively isolates high-frequency risk signatures—which represent only 0.41% of the total energy yet capture extreme meteorological forcing—from the dominant low-frequency seepage trend, significantly outperforming baseline models and pre-positioned attention variants.

(3) Strategic significance and future outlook: This research provides a paradigm shift in risk management for data-scarce karst regions, advocating a transition from passive sealing to proactive, mechanism-driven early warning. While the integrated model delivers robust outputs, the internal interaction weights among decomposed components warrant further investigation to achieve full model transparency. Future work will prioritize developing Explainable AI frameworks to map attention weights directly to physical hydraulic parameters, as well as exploring model lightweighting for real-time edge computing on construction sites.

Acknowledgements

This work was supported by the National Natural Science Foundation of China (U2267218; 42472308；42377050；42477066) and the Special Study on Hydrogeology of Underground Pumping Station Factory Area in Xiaolangdi Yellow River Diversion Project, Shanxi Province.

References

1. Luo, M., Chen, J., Jakada, H., Li, N., Guo, X., Zhou, H.: Identifying and predicting karst water inrush in a deep tunnel, South China. Eng. Geol. 305, 106716 (2022). https://doi.org/10.1016/j.enggeo.2022.106716
2. Chen, Z., Su, Z., Li, M., Shen, Q., Fan, L., Zhang, Y.: Investigation of the Tunnel Water Inflow Prediction Method Based on the MODFLOW-DRAIN Module. Water (Switzerland) 16, (2024). https://doi.org/10.3390/w16081078
3. Li, S. cai, He, P., Li, L. ping, Shi, S. shuai, Zhang, Q. qing, Zhang, J., Hu, J.: Gaussian process model of water inflow prediction in tunnel construction and its engineering applications. Tunn. Undergr. Sp. Technol. 69, 155–161 (2017). https://doi.org/10.1016/j.tust.2017.06.018
4. Shi, S., Guo, W., Li, S., Xie, X., Li, X., Zhao, R., Xue, Y., Lu, J.: Prediction of tunnel water inflow based on stochastic deterministic three-dimensional fracture network. Tunn. Undergr. Sp. Technol. 135, 104997 (2023). https://doi.org/10.1016/j.tust.2023.104997
5. Song, W.K., Hamm, S.Y., Cheong, J.Y.: Estimation of groundwater discharged into a tunnel. Tunn. Undergr. Sp. Technol. 21, 460 (2006). https://doi.org/10.1016/j.tust.2005.12.098
6. Chi, W., Ma, L., Qian, J., Fang, Y., Luo, Q., Liu, Y.: Integrating multiple methods to identify groundwater runoff characteristics in karst water inflow areas of an underground pumping station in North China. J. Hydrol. 663, (2025). https://doi.org/10.1016/j.jhydrol.2025.134198
7. Wang, Y., Zheng, S., Zhong, Z., Li, Y., Li, Z.: Transportation Geotechnics Experimental investigation on the hydraulic characteristics of water inrush in deep buried filled karst conduit considering the permeability. Transp. Geotech. 43, 101115 (2023). https://doi.org/10.1016/j.trgeo.2023.101115
8. Zhang, X., Wang, M., Feng, D., Wang, J.: Water Inflow Amount Prediction for Karst Tunnel with Steady Seepage Conditions. Sustain. 15, (2023). https://doi.org/10.3390/su151310638
9. Mao, Y., Zhang, X., Zhang, Z., Tao, Z., He, M.: Tunnelling and Underground Space Technology incorporating Trenchless Technology Research Research on genesis , evolution and prevention of water and mud inrush in the non-karst tunnel : A case study in Yunnan , southwest China. Tunn. Undergr. Sp. Technol. Inc. Trenchless Technol. Res. 166, 106967 (2025). https://doi.org/10.1016/j.tust.2025.106967
10. Li, L.P.: Evolution Mechanism of Water Inrush Disaster in High-risk Karst Tunnels and Its Application Research. Doctoral dissertation, Shandong University (2009). [In Chinese]. https://kns.cnki.net/kcms2/article/abstract?v=mg_qcPBBapkq5jnK_6xkxV8mvxzLSbCSrkqTQqCj44GPaDZrzQs0SYaRsB6jHk7FZrEU1d4m5mUfm556wRWjcvvpdckzCHmchep2QbyDR7NNOiLaChR8PuhuJTKYk5Nwxrhx-ygaKP-2Rp4s5ean8IgGaazOJhaaA55jLJI2D6_75SP-qqiz3A==&uniplatform=NZKPT&language=CHS
11. Xue, Y., Kong, F., Li, S., Qiu, D., Su, M., Li, Z.: Tunnelling and Underground Space Technology incorporating Trenchless Technology Research Water and mud inrush hazard in underground engineering : Genesis , evolution and prevention. Tunn. Undergr. Sp. Technol. Inc. Trenchless Technol. Res. 114, 103987 (2021). https://doi.org/10.1016/j.tust.2021.103987
12. Zuo, Q.K.: Study on Mechanism and Prevention Measures of Water Inrush in Dasha Highway Tunnel. Master's thesis, Chengdu University of Technology (2011). [In Chinese]. https://kns.cnki.net/kcms2/article/abstract?v=mg_qcPBBapnWO9LiQFR3wjzu44RYOe7fWdIg0Cqv2GYFvBzoymO9mA82LYCJh-PNcjsjRu973ilpjf0RVhzsHOwjIdqFwMOeTKGer0qiIVPQ1UPc--aVGLqFhhwFvEPSP7v9puSNiIyNui-lDB9Iaxaj7UuSToBtYAxYr9tkFiSRu2I9Tn9ZRQ==

&uniplatform=NZKPT&language=CHS
13. Jin, X., Subramaniam, B., Chaudhari, R.V., Thapa, P.S.: Kinetic modeling of Pt/C catalyzed aqueous phase glycerol conversion with in situ formed hydrogen. AIChE J. 62, 1162-1173 (2016). https://doi.org/10.1002/aic.15114
14. Lin, P., Li, S.C., Xu, Z.H., Wang, J., Huang, X.: Water inflow prediction during heavy rain while tunneling through Karst fissured zones. Int. J. Geomech. 19(8), 04019093 (2019). https://doi.org/10.1061/(ASCE)GM.1943-5622.0001478
15. Shi, S., Bu, L., Li, S., Xiong, Z., Xie, X., Li, L., Zhou, Z., Xu, Z., Ma, D.: Application of comprehensive prediction method of water inrush hazards induced by unfavourable geological body in high risk karst tunnel: a case study. Geomatics, Nat. Hazards Risk 8, 1407 – 1423 (2017). https://doi.org/10.1080/19475705.2017.1337656
16. Frame, J.M., Kratzert, F., Klotz, D., Gauch, M., Shelev, G., Gilon, O., Qualls, L.M., Gupta, H.V., Nearing, G.S.: Deep learning rainfall-runoff predictions of extreme events. Hydrol. Earth Syst. Sci. 26, 3377 – 3392 (2022). https://doi.org/10.5194/hess-26-3377-2022
17. An, L., Hao, Y., Yeh, T.C.J., Liu, Y., Liu, W., Zhang, B.: Simulation of karst spring discharge using a combination of time – frequency analysis methods and long short-term memory neural networks. J. Hydrol. 589, 125320 (2020). https://doi.org/10.1016/j.jhydrol.2020.125320
18. Mahmoodzadeh, A., Ghafourian, H., Hussein, A., Rezaei, N., Hashim, H., Rashidi, S.: Transportation Geotechnics Predicting tunnel water inflow using a machine learning-based solution to improve tunnel construction safety. Transp. Geotech. 40, 100978 (2023). https://doi.org/10.1016/j.trgeo.2023.100978
19. Zhang, X., Peng, Y., Zhang, C., Wang, B.: Are hybrid models integrated with data preprocessing techniques suitable for monthly streamflow forecasting? Some experiment evidences. J. Hydrol. 530, 137 – 152 (2015). https://doi.org/10.1016/j.jhydrol.2015.09.047
20. He, Z., Wen, X., Liu, H., Du, J.: A comparative study of artificial neural network, adaptive neuro fuzzy inference system and support vector machine for forecasting river flow in the semiarid mountain region. J. Hydrol. 509, 379 – 386 (2014). https://doi.org/10.1016/j.jhydrol.2013.11.054
21. Hu, F., Yang, Q., Yang, J., Shao, J., Wang, G.: An adaptive rainfall-runoff model for daily runoff prediction under the changing environment: Stream-LSTM. Environ. Model. Softw. 191, 106524 (2025a). https://doi.org/10.1016/j.envsoft.2025.106524
22. Hu, Y., Li, H., Zhang, C., Wang, T., Chu, W., Li, R.: Investigate the rainfall-runoff relationship and hydrological concepts inside LSTM. Environ. Model. Softw. 192, 106527 (2025b). https://doi.org/10.1016/j.envsoft.2025.106527
23. Guo, J., Zhou, J., Qin, H., Zou, Q., Li, Q.: Monthly streamflow forecasting based on improved support vector machine model. Expert Syst. Appl. 38(10), 13073 – 13081 (2011). https://doi.org/10.1016/j.eswa.2011.04.114
24. Cui, D.W.: Application of hidden multilayer BP neural network model in runoff prediction. J. China Hydrol. 33(1), 68 – 73 (2013). (in Chinese)
25. Hu, C., Hao, Y., Yeh, T.C.J., Pang, B., Wu, Z.: Simulation of spring flows from a karst aquifer with an artificial neural network. Hydrol. Proc. 22(5), 596-604 (2008). https://doi.org/10.1002/hyp.6625
26. Khaldi, R., El Afia, A., Chiheb, R., Tabik, S.: What is the best RNN-cell structure to forecast each time series behavior? Expert Syst. Appl. 215, 119140 (2023). https://doi.org/10.1016/j.eswa.2022.119140

27. Shi, J., Wang, S., Qu, P., Shao, J.: Time series prediction model using LSTM-Transformer neural network for mine water inflow. Sci. Rep. 14, 1 – 16 (2024). https://doi.org/10.1038/s41598-024-69418-z
28. Kim, Y.D., Durlofsky, L.J.: Convolutional – recurrent neural network proxy for robust optimization and closed-loop reservoir management. Comput Geosci 27, 179 – 202 (2023). https://doi.org/10.1007/s10596-022-10189-9
29. Yin, H., Wu, Q., Yin, S., Dong, S., Dai, Z., Soltanian, M.R.: Predicting mine water inrush accidents based on water level anomalies of borehole groups using long short-term memory and isolation forest. J. Hydrol. 616, 128813 (2023). https://doi.org/10.1016/j.jhydrol.2022.128813
30. Hu, C., Wu, Q., Li, H., Jian, S., Li, N., Lou, Z.: Deep learning with a long short-term memory networks approach for rainfall-runoff simulation. Water (Switzerland) 10, 1 – 16 (2018). https://doi.org/10.3390/w10111543
31. Huang, X., Gao, L., Zhang, N., Crosbie, R.S., Ye, L., Liu, J., Guo, Z., Meng, Q., Fu, G., Bryan, B.A.: A top-down deep learning model for predicting spatiotemporal dynamics of groundwater recharge. Environ. Model. Softw. 167, 105778 (2023). https://doi.org/10.1016/j.envsoft.2023.105778
32. Huang, X., Gao, L., Crosbie, R.S., Zhang, N., Fu, G., Doble, R.: Groundwater Recharge Prediction Using Linear Regression, Multi-Layer Perception Network, and Deep Learning. Water 11, 1879 (2019). https://doi.org/10.3390/w11091879
33. Koohmishi, M., Connolly, D.P.: Railway Ballast Fouling Detection using Thermal Imaging: Integration of LSTM and XGBoost. Transp. Geotech. 101889 (2025). https://doi.org/10.1016/j.trgeo.2025.101889
34. Bian, J., Hou, T., Ren, D., Lin, C., Qiao, X., Ma, X., Ma, J., Wang, Y., Wang, J., Liang, X.: Predicting mine water inflow volumes using a decomposition-optimization algorithm-machine learning approach. Sci. Rep. 14, 1 – 18 (2024). https://doi.org/10.1038/s41598-024-67962-2
35. Liu, F., Cai, M., Wang, L., Lu, Y.: An Ensemble Model Based on Adaptive Noise Reducer and Over-Fitting Prevention LSTM for Multivariate Time Series Forecasting. IEEE Access 7, 26102 – 26115 (2019). https://doi.org/10.1109/ACCESS.2019.2900371
36. Padilla, A., Pulido-Bosch, A.: Study of hydrographs of karstic aquifers by means of correlation and cross-spectral analysis. J. Hydrol. 168, 73 – 89 (1995). https://doi.org/10.1016/0022-1694(94)02648-U
37. Ahmed, A.A., Sayed, S., Abdoulhalik, A., Moutari, S., Oyedele, L.: Applications of machine learning to water resources management: A review of present status and future opportunities. J. Clean. Prod. 441, 140715 (2024). https://doi.org/10.1016/j.jclepro.2024.140715
38. Liu, G., Guo, J.: Bidirectional LSTM with attention mechanism and convolutional layer for text classification. Neurocomputing 337, 325 – 338 (2019). https://doi.org/10.1016/j.neucom.2019.01.078/;
39. Lai, F.L., Gao, F.: LSA-ac4C: A hybrid neural network incorporating double-layer LSTM and self-attention mechanism for the prediction of N4-acetylcytidine sites in human mRNA. Int. J. Biol. Macromol. 253, 126837 (2023). https://doi.org/10.1016/j.ijbiomac.2023.126837
40. Wang, Z., Liu, N., Chen, C., Guo, Y.: Adaptive self-attention LSTM for RUL prediction of lithium-ion batteries. Inf. Sci. (Ny). 635, 398 – 413 (2023). https://doi.org/10.1016/j.ins.2023.01.100
41. Ministry of Housing and Urban-Rural Development of the People's Republic of China: Standard

for engineering classification of rock mass: GB/T 50218—2014[S]. Beijing: China Planning Press (2014)
42. Torres, M.E., Colominas, M.A., Schlotthauer, G., Flandrin, P.: A complete ensemble empirical mode decomposition with adaptive noise. ICASSP, IEEE Int. Conf. Acoust. Speech Signal Process. - Proc. 4144 – 4147 (2011). https://doi.org/10.1109/ICASSP.2011.5947265
43. Jayaparvathy, R., Daphin Lilda, S., Sheeba Angel, A., Rajasekaran, A.: Soil moisture prediction based on integrating the CEEMDAN decomposition technique with LSTM in the proximity of Prosopis Juliflora. J. Hydrol. 640, 131777 (2024). https://doi.org/10.1016/j.jhydrol.2024.131777
44. Cai, X., Yuan, B., Wu, C.: An integrated CEEMDAN and TCN-LSTM deep learning framework for forecasting. Int. Rev. Financ. Anal. 98, 103879 (2025). https://doi.org/10.1016/j.irfa.2024.103879
45. Chai, Q., Zhang, S., Tian, Q., Yang, C., Guo, L.: Daily Runoff Prediction Based on FA-LSTM Model. Water (Switzerland) 16, (2024). https://doi.org/10.3390/w16162216
46. Qin, W., Tang, J., Lu, C. et al.: Trajectory prediction based on long short-term memory network and Kalman filter using hurricanes as an example. Comput Geosci 25, 1005 – 1023 (2021). https://doi.org/10.1007/s10596-021-10037-2
47. Vural, N.M., Ilhan, F., Yilmaz, S.F., Ergut, S., Kozat, S.S.: Achieving Online Regression Performance of LSTMs With Simple RNNs. IEEE Trans. Neural Networks Learn. Syst. 33, 7632 – 7643 (2022). https://doi.org/10.1109/TNNLS.2021.3086029
48. Hochreiter, S., Schmidhuber, J.: Long short-term memory. Neural Comput. 9(8), 1735-1780 (1997). https://doi.org/10.1162/neco.1997.9.8.1735
49. Subakan, C., Ravanelli, M., Cornell, S., Grondin, F., Bronzi, M.: Exploring Self-Attention Mechanisms for Speech Separation. IEEE/ACM Trans. Audio Speech Lang. Process. 31, 2169 – 2180 (2023). https://doi.org/10.1109/TASLP.2023.3282097
50. Li, Y., Zhu, Z., Kong, D., Han, H., Zhao, Y.: EA-LSTM: Evolutionary attention-based LSTM for time series prediction. Knowledge-Based Syst. 181, 104785 (2019). https://doi.org/10.1016/j.knosys.2019.05.028
51. Meng, E., Huang, S., Huang, Q., Fang, W., Wu, L., Wang, L.: A robust method for non-stationary streamflow prediction based on improved EMD-SVM model. J. Hydrol. 568, 462 – 478 (2019). https://doi.org/10.1016/j.jhydrol.2018.11.015